JOURNAL OF Materials CHEMISTRY

Zr substituted bismuth uranate

Rose-Noëlle Vannier,*[a] Odile Théry,[a] Christophe Kinowski,[a] Marielle Huvé,[a] Gustaaf Van Tendeloo,[b] Emmanuelle Suard[c] and Francis Abraham[a]

[a] *Laboratoire de Cristallochimie et Physicochimie du Solide, ENSCL , BP 108, 59652 Villeneuve d'Ascq Cedex, France. E-mail: vannier@ensc-lille.fr*
[b] *EMAT , University of Antwerp (RUCA), Groenenborgerlaan 171, B-2020 Antwerp, Belgium*
[c] *Institut Laue Langevin, Avenue des Martyrs, BP 156, 38042 Grenoble Cedex 9, France*

Received 27th July 1998, Accepted 30th October 1998

A $Bi_2U_{1-x}Zr_xO_{6-x}$ solid solution has been evidenced for $0 \leqslant x \leqslant 0.40$. The monoclinic Bi_2UO_6 room-temperature form extends in the range $0 \leqslant x \leqslant 0.20$ and the related trigonal high Bi_2UO_6 form is stabilised at room temperature for higher substitution ratio. The electrical properties of these materials have been measured. Neutron diffraction combined with electron diffraction microscopy allow proposal of a structural model and confirmed the two dimensional properties of these materials.

Introduction

Bi_2O_3 based solid electrolytes are well known for their high oxide ion conduction properties.[1] Among these materials the BIMEVOX family of compounds have led to an increasing interest during the last ten years.[2] They derive from $Bi_2VO_{5.5}$ by substitution of vanadium by numerous metals.[3] Their average structure is related to that of the first member of the Aurivillius family *i.e.* Bi_2WO_6 [Fig. 1(a)]. It consists of $Bi_2O_2^{2+}$ sheets alternating with $(VO_{3.5}\square_{0.5})^{2-}$ oxygen deficient perovskite slabs.[4] The layer structure and the presence of oxygen vacancies in the perovskite slabs lead to high oxide anion conduction.

In contrast, Bi_2WO_6 that contains no oxygen vacancies, is a very poor conductor; its conduction properties are however significantly enhanced by substitution of W^{VI} by Ta^V or Nb^V.[5]

The bismuth uranate Bi_2UO_6, is another layer compound which presents very interesting conduction properties.[6] Its structure has been solved by Koster *et al.*[7] It consists of a stacking of slabs of edge-sharing UO_8 polyhedra sandwiched between $Bi_2O_2^{2+}$ sheets and is compared to that of Bi_2WO_6 in Fig. 1. Although their formulations are the same, in both compounds the $Bi_2O_2^{2+}$ layers are structurally very different. The first, found in the Aurivillius family, are built up from a plane of oxygen with bismuth atoms alternately up and down,

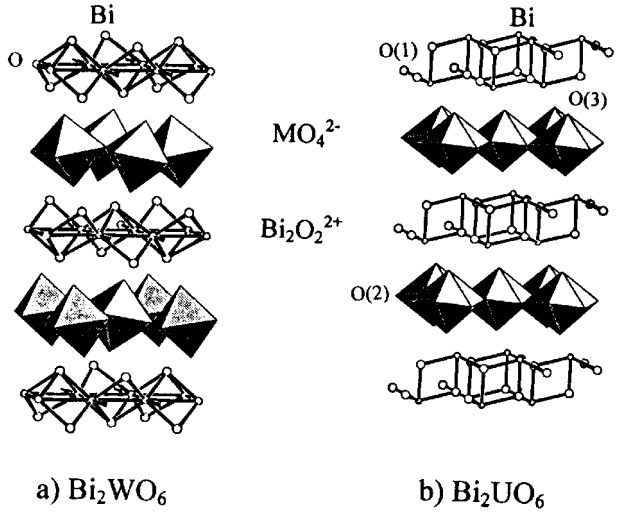

Fig. 1 (a) Bi_2WO_6 structure compared to (b) Bi_2UO_6 model proposed by Koster *et al.*[7]

whereas the second can be viewed as double BiO sheets. Depending on the temperature Bi_2UO_6 displays two polymorphs: a monoclinic form at 20 °C that crystallises in the *C*2 space group with $a = 6.872(2)$ Å, $b = 4.009(1)$ Å, $c = 9.690(3)$ Å, $\beta = 90.16(1)^\circ$ and a trigonal fluorite-like structure stable above 800 °C, with space group $P\bar{3}$ and $a = 4.045(5)$ Å, $c = 9.90(1)$ Å (at 1000 °C). The low temperature form is in fact a monoclinic distortion of the orthorhombic C lattice corresponding to the hexagonal form.

Although the two dimensional properties of this compound have not been demonstrated, the high oxygen ion conduction of this material is also likely to be related to its layer structure. Bonanos suggested that oxygen O(2) in the Bi–O layers and possibly O(3) oxide site could be responsible for the conduction and suggested the existence of interstitial oxygen in the Bi–O layers.[6]

Owing to the similarities in the structures and properties of $Bi_2VO_{5.5}$ or Bi_2WO_6 on one hand and Bi_2UO_6 on the other, the $Bi_2VO_{5.5}$–Bi_2UO_6 and Bi_2WO_6–Bi_2UO_6 systems have been investigated. Two solid solutions with BIMEVOX and Bi_2WO_6 structural types have been evidenced respectively.[8,9] However V^V and W^{VI} did not substitute for uranium in the bismuth uranate.

Consequently, several other attempts for doping this uranate were carried out. Only zirconium led to the stabilisation of a $Bi_2U_{1-x}Zr_xO_{6-x}$ solid solution which has been characterised by X-ray diffraction and electrical measurements have been performed. Neutron diffraction combined with electron microscopy enabled us to propose preferential migration pathways for oxygen in these materials.

Experimental

Syntheses were carried out by the classical solid-state method. About 2 g of polycrystalline samples were prepared from appropriate amounts of stoichiometric mixtures of reagents: Bi_2O_3 (Riedel de Haën, 99.5%), $UO_3{\cdot}H_2O$ (CEA), ZrO_2 (Riedel de Haën 99%). The reactants were thoroughly mixed in an agate mortar and fired in Au foil boats successively at 500, 800 and 850 °C. For neutron diffraction, larger amounts (*ca.* 25 g) of powder were prepared and mixtures were ball milled using an alumina mortar. In these experiments, U_3O_8 (Prolabo >99%) and $C_{20}H_{28}O_8Zr$, zirconium acetylacetonate, (Merck >98%) were used to prepare $Bi_2U_{0.9}Zr_{0.1}O_{5.9}$ and $Bi_2U_{0.65}Zr_{0.35}O_{5.65}$ and gold foil boats were replaced by alumina crucibles.

The phases were characterised by X-ray diffraction (Guinier

De Wolff camera and Siemens D5000 goniometer, Cu-Kα radiation) in the range $10 \leqslant 2\theta \leqslant 70^\circ$ using a 4 s counting time. Owing to the complexity of the diffractograms containing numerous multiplets, unit cell parameters were refined using the Fullprof program in pattern-matching mode.[10]

Densities were measured using a Micromeritics Accupyc 1330 helium pycnometer with a 1 ml sample capacity. Ionic conductivity measurements were performed in air with an S.I. 1225 frequency analyser (Schlumberger) in the frequency range $1–10^6$ Hz. Two heating–cooling cycles were carried out between 200 and 800 °C in steps of 20 °C with 1 h stabilisation allowed before each complex impedance measurement. Samples were cylindrical pellets (5 mm diameter) previously sintered at 865 °C for 12 h, to which sputtered gold electrodes were attached.

Neutron diffraction data were collected at room temperature on the high resolution powder diffractometer D2B at the Institut Laue Langevin (I.L.L.) at Grenoble. Approximately 20 g of compound were placed in a 15 mm diameter cylindrical vanadium can and data were collected in the range $0 \leqslant 2\theta \leqslant 161.95^\circ$ at a wavelength of $\lambda = 2.397$ Å using a graphite filter. The detector bank was stepped in 0.05° intervals in 2θ and the resulting intensities were normalised with respect to detector efficiency and positional errors. The Fullprof program was used for the refinement, only data in the range $10 \leqslant 2\theta \leqslant 150^\circ$ were taken into account.

Electron diffraction was performed on a JEOL 200CX electron microscope equipped with an eucentric goniometer ($\pm 60^\circ$), high resolution images were obtained on a JEOL 4000Ex with point resolutions of 1.7 Å and EDX analysis was carried out on a Phillips CM30. The material was crushed and dispersed on a holey carbon film deposited on a Cu grid. The computer-simulated images were calculated using a Mac Tempas program.

Results and discussion

$Bi_2U_{1-x}Zr_xO_{6-x}$ solid solution

$Bi_2U_{1-x}Zr_xO_{6-x}$ compounds have been synthesised with intervals in x of 0.05. Typical X-ray diffraction patterns are shown in Fig. 2. Clearly a solid solution is observed within the range $0 \leqslant x \leqslant 0.40$. For higher substitution ratios extra lines corresponding to a δ-Bi_2O_3 (* on Fig. 2) and ZrO_2 are evidenced. A shrinking of the width of the diffraction lines is noticed for $x > 0.20$, indicating a possible stabilisation at room temperature of the high temperature Bi_2UO_6 polymorph by zirconium substitution.

As a first step, unit cell parameters were refined in the $C2$ space group for each composition. The convergence of β to 90° and of $a/\sqrt{3}$ to b for $x \approx 0.25$, confirmed the stabilisation at room temperature of the high temperature polymorph by zirconium substitution. Therefore, in a second step, parameters

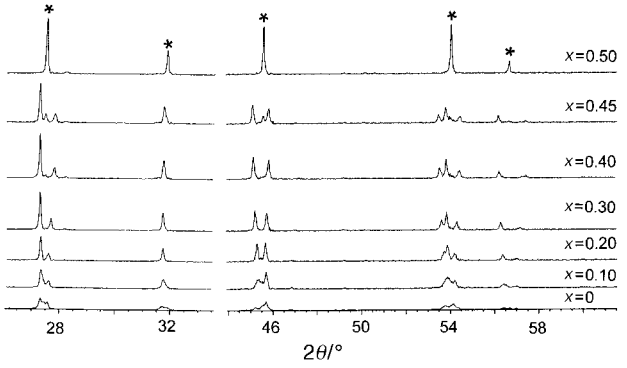

Fig. 2 Typical X-ray diffraction patterns corresponding to $Bi_2U_{1-x}Zr_xO_{6-x}$ compositions ($0 \leqslant x \leqslant 0.50$) (* indicate δ-$Bi_2O_3$ lines).

Table 1 $Bi_2U_{1-x}Zr_xO_{6-x}$ cell parameters refined from X-ray diffraction data and calculated densities compared to the experimental values

x	a/Å	b/Å	c/Å	β/°	D_c/ g cm^{-3} [a]	D_m/ g cm^{-3}
0	6.885(1)	4.0081(6)	9.696(2)	90.23(2)	9.34	9.24(3)
0.05	6.887(2)	4.0034(6)	9.692(2)	90.13(2)	9.25	9.23(3)
0.10	6.904(2)	4.0003(6)	9.690(2)	90.11(2)	9.13	9.12(3)
0.15	6.918(2)	4.0003(6)	9.690(2)	90.07(2)	9.01	9.02(3)
0.20	6.926(2)	4.0004(5)	9.688(1)	90.05(2)	8.90	8.95(3)
0.25	4.0055(5)		9.677(2)		8.79	8.88(3)
0.30	4.0072(5)		9.662(2)		8.69	8.77(3)
0.35	4.0124(4)		9.642(1)		8.59	8.73(3)
0.40	4.0131(6)		9.629(2)		8.50	8.45(3)

[a] Calculated assuming two $Bi_2U_{1-x}Zr_xO_{6-x}$ units per cell for monoclinic forms and one for trigonal forms (N.B. standard deviations given by Fullprof program have been multiplied by a factor of two).

corresponding to these compositions were refined in the $P\bar{3}$ space group (Table 1). The evolution of $a/\sqrt{3}$, b and c parameters is shown in Fig. 3; the $a/\sqrt{3}$ parameter clearly converges to b for $x \geqslant 0.25$ and c suddenly decreases.

Densities have been measured and are reported in Table 1. They are in good agreement with the hypothesis of zirconium substituting for uranium.

Conductivity measurements

Conductivity measurements have been performed. As no difference between heating and cooling processes was observed, only values corresponding to the second cooling cycle are shown in Fig. 4. Activation energies are reported in Table 2.

In the case of non-doped material a continuous slope change

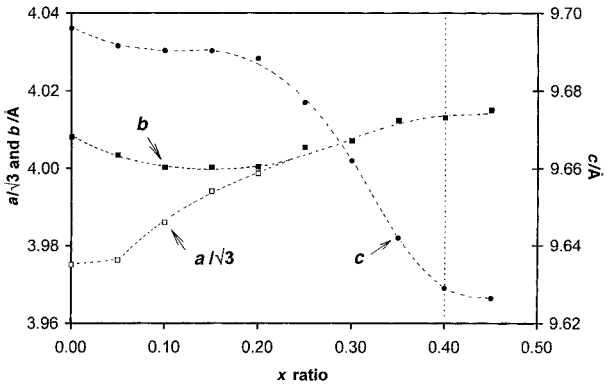

Fig. 3 Cell parameters evolution as a function of composition refined from X-ray diffraction data.

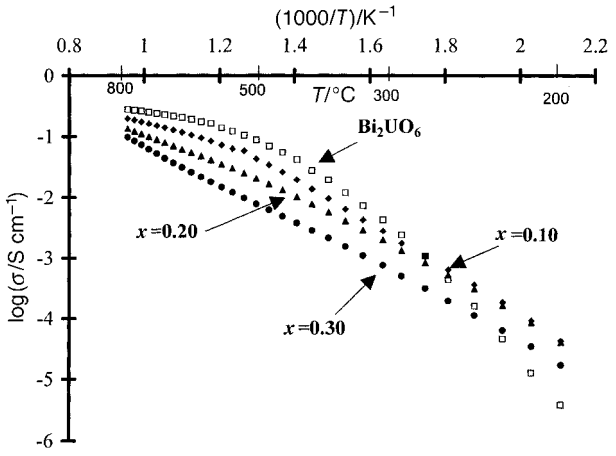

Fig. 4 Conductivity *versus* reciprocal temperature plots for $Bi_2U_{1-x}Zr_xO_{6-x}$.

Table 2 $Bi_2U_{1-x}Zr_xO_{6-x}$ activation energies in eV

x	Above 500 °C	Below 500 °C
0	0.2	1.3
0.10	0.3	0.8
0.20	0.5	0.7
0.30	0.7	

of $\log \sigma = f(10^3/T)$ plot is seen. An activation energy of 0.2 eV is calculated above 500 °C *cf.* 1.3 eV below this temperature. Similar behaviour has already been observed for BIMEVOX materials and Nb or Ta substituted Bi_2WO_6 and is assumed to be related to an order–disorder phase transformation due to the existence of dopant–vacancy pair interactions at low temperature.[11]

The same slope change is observed for the $x=0.10$ and 0.20 monoclinic compounds while only one domain is seen for the trigonal $x=0.30$ composition with an activation energy of 0.7 eV. The performances of these materials decrease as the substitution ratio increases.

Neutron diffraction

To understand the oxygen migration pathways in these materials, neutron diffraction experiments have been performed on the undoped bismuth uranate and on two zirconium substituted compounds: a monoclinic form ($x=0.10$) and a trigonal form ($x=0.35$).

Powders were previously checked by X-ray diffraction and while no impurity was detected, neutron diffraction clearly revealed the presence of an extra phase, as confirmed by EDS and X-ray fluorescence analyses with traces of alumina evidenced. However, an EDX analysis performed on crystals, revealed no contamination of the bismuth uranate and the powders had probably been contaminated by ball milling. Therefore, the presence of corundum was taken into account in the refinements.

In a first step, data corresponding to non-doped bismuth uranate were refined using Koster's model. An overall thermal parameter was used and gave rise to the following reliability factors: $R_B=9.76\%$ and $R_F=7.96\%$ comparable to Koster's value of $R=10\%$. At this stage a Fourier difference synthesis was performed and revealed a maximum at 0, 0.16, 1/2.

Therefore, in a second step this extra oxygen site, labelled O(2b), was introduced. Refinement of oxygen occupancies gave rise to 0.872(6), 0.878(5), 0.185(2) and 1.02(4) for O(1), O(2), O(2b) and O(3) respectively. Assuming U^{VI}, 0.13 oxygen atom were still missing, but a new Fourier difference synthesis revealed an extra maximum at 1/2, 0, 0. Therefore an extra site O(1b) was introduced in the refinement, and the following oxygen occupancies were obtained : 0.687(4), 0.23(2), 0.97(5), 0.20(2) and 1.02(4) for O(1), O(1b), O(2), O(2b) and O(3) respectively.

At this stage, it was obvious that no vacancy was present on the O(3) site. A too short O(1)–O(1b) bond length precludes the simultaneous occupancy of two O(1) for one O(1b), therefore the occupancies of these two sites were constrained so that one O(1b) would substitute for 2O(1). This led to a final oxygen stoichiometry of 5.95(4) very close to the expected value (6) assuming Bi^{III} and U^{VI}.

Final results are reported in Table 3 and the calculated pattern is compared to the experimental one in Fig. 5.

Consequently $Bi_2U_{0.9}Zr_{0.1}O_{5.9}$ was refined using the same approach. Final results are reported in Table 4 and Fig. 6. A 5.8(1) oxygen stoichiometry was obtained, in excellent accordance with the expected 5.9 assuming Bi^{III}, U^{VI} and Zr^{IV}.

Finally $Bi_2U_{0.65}Zr_{0.35}O_{5.65}$ was refined in the $P\bar{3}$ space group using the model proposed by Koster for the high temperature form of Bi_2UO_6.[7] A Fourier difference synthesis was performed and revealed an extra site at 1/2, 0, 0. An extra O(1b) site was therefore introduced and final results are reported in Table 5 and in Fig. 7. In this case ZrO_2 was also taken into account as an impurity.

Important bond lengths are reported in Table 6; bond valences have been calculated according to data from Brown and Altermatt.[12]

The layer structure of these materials is confirmed. As in the previous model,[7] bismuth atoms form double BiO sheets with O(2) and O(2b) oxygen atoms, but, depending on the substitution ratio, the oxygen content of these sheets varies from 2.34 to 2. Bismuth atoms exhibit a classical one sided coordination, characteristic of Bi^{3+} with its stereochemically active $6s^2$ lone pair. Depending on the presence or not of an

Table 3 Structural parameters for Bi_2UO_6 from neutron diffraction data[a]

Atom	Site	x	y	z	Occupancy factor × normalised multiplicity
Bi	4c	0.664(2)	−0.008(7)	0.3605(6)	1
U	2a	0	0	0	0.5
O(1)	4c	0.683(4)	−0.06(2)	0.008(2)	0.60(2)
O(1b)	2a	1/2	−0.06(2)	0	0.20(2)
O(2)	4c	0.683(2)	0.01(2)	0.583(2)	0.94(3)
O(2b)	2b	0	0.13(2)	1/2	0.23(2)
O(3)	4c	−0.004(4)	−0.00(1)	0.194(2)	1

[a]Space group $C2$, $B_{ov}=2.22(5)$ Å^{-2}; $a=6.8782(8)$ Å, $b=4.0057(4)$ Å, $c=9.6939(9)$ Å, $\beta=90.11(1)°$, $R_p=6.14\%$, $R_{wp}=8.49\%$, $R_E=2.41\%$, $R_B=4.31\%$, $R_F=3.35\%$. N.B. standard deviations given by Fullprof program have been multiplied by a factor of two.

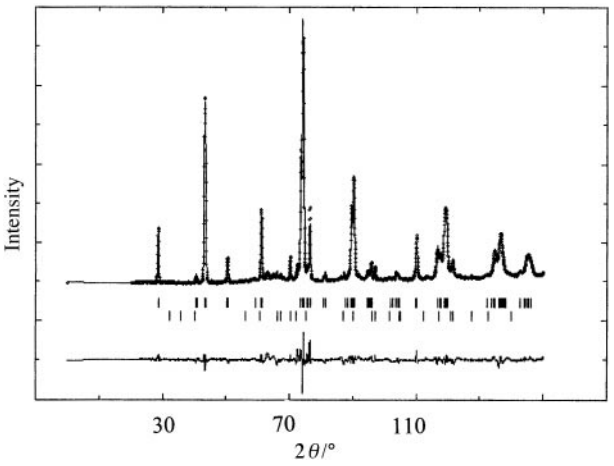

Fig. 5 Bi_2UO_6 neutron diffraction calculated pattern compared to the experimental one (the first line of tick marks is related to Bi_2UO_6 reflections and the second to the corundum impurity).

Table 4 Structural parameters for $Bi_2U_{0.9}Zr_{0.1}O_{5.9}$ from neutron diffraction data[a]

Atom	Site	x	y	z	Occupancy
Bi	4c	0.664(2)	0.01(1)	0.3561(6)	1
U/Zr	2a	0	0	0	0.45/0.05
O(1)	4c	0.677(4)	−0.03(2)	0.015(2)	0.64(2)
O(1b)	2a	1/2	−0.05(2)	0	0.18(2)
O(2)	4c	0.678(3)	0.05(7)	0.581(2)	0.93(4)
O(2b)	2b	0	0.17(2)	1/2	0.16(2)
O(3)	4c	−0.012(4)	0.04(2)	0.198(2)	1

[a]Space group $C2$, $B_{ov}=1.83(5)$ Å^{-2}; $a=6.8949(8)$ Å, $b=4.0051(5)$ Å, $c=9.691(1)$ Å, $\beta=90.08(2)°$, $R_p=6.87\%$, $R_{wp}=9.82\%$, $R_E=2.16\%$, $R_B=5.59\%$, $R_F=4.42\%$. N.B. standard deviations given by Fullprof program have been multiplied by a factor of two.

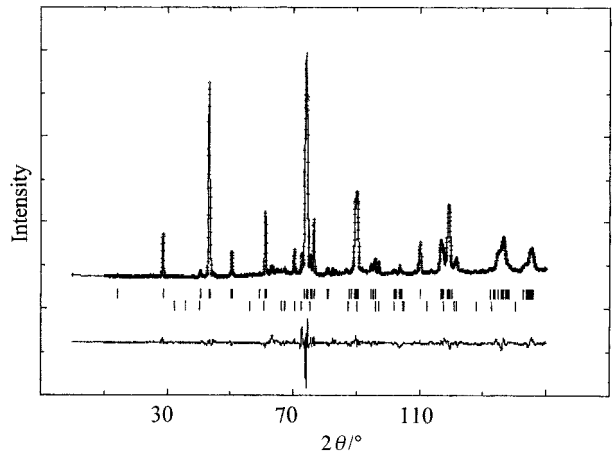

Fig. 6 $Bi_2U_{0.9}Zr_{0.10}O_{5.9}$ neutron diffraction calculated pattern compared to the experimental one (the first line of tick marks is related to $Bi_2U_{0.9}Zr_{0.10}O_{5.9}$ reflections and the second to the corundum impurity).

Table 5 Structural parameters for $Bi_2U_{0.65}Zr_{0.35}O_{5.65}$ from neutron diffraction data[a]

Atom	Site	x	y	z	Occupancy
Bi	2d	2/3	1/3	0.3471(5)	1
U/Zr	1a	0	0	0	0.325/0.175
O(1)	2d	2/3	1/3	0.022(2)	0.59(2)
O(1b)	3e	1/2	0	0	0.27(2)
O(2)	2d	2/3	1/3	0.5705(6)	1
O(3)	2c	0	0	0.2087(8)	1

[a]Space group $P\bar{3}$, $B_{ov}=0.75(2)$ Å^{-2}; $a=4.0136(2)$ Å, $c=9.6474(5)$ Å, $R_p=5.37\%$, $R_{wp}=7.46\%$, $R_E=2.38\%$, $R_B=6.59\%$, $R_F=5.17\%$. N.B. standard deviations given by Fullprof program have been multiplied by a factor of two.

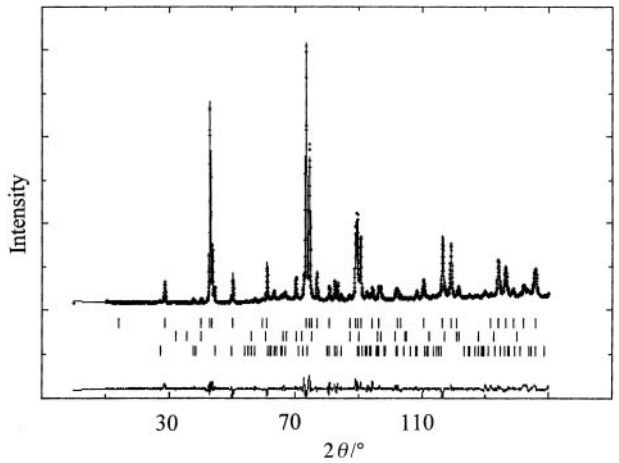

Fig. 7 $Bi_2U_{0.65}Zr_{0.35}O_{5.65}$ calculated pattern compared to the experimental one (the first line of tick marks is related to $Bi_2U_{0.65}Zr_{0.35}O_{5.65}$ reflections, the second to the corundum impurity and the third to ZrO_2 impurity).

O(2b) site in the surrounding structure, two or three short Bi–O bond lengths (<2.3 Å) are observed.

A projection of oxygen atoms located in one double BiO sheet along [0 0 1] at $z=1/2$ is shown in Fig. 8. The presence of the extra O(2b) site can explain possible oxygen migration in these slabs. Two small O(2)–O(2b) bond lengths of 2.38(2) and 2.13(5) Å are observed, such short distances have already been observed for interstitial oxygen between (LaO) layers in the superconductor $La_2NiO_{4+\delta}$.[13–15]

Therefore a preferred oxygen migration pathway, drawn as a dotted line in Fig. 8, can be proposed. Of course this migration pathway disappears in the $x=0.35$ trigonal form where the O(2b) site is absent, and migration through the Bi–O sheet in this compound appears to be impossible.

Table 6 Main bond lengths (in Å) corresponding to Bi_2UO_6, $Bi_2U_{0.9}Zr_{0.1}O_{5.9}$ and $Bi_2U_{0.65}Zr_{0.35}O_{5.65}$[a]

	Bi_2UO_6	$Bi_2U_{0.9}Zr_{0.1}O_{5.9}$	$Bi_2U_{0.65}Zr_{0.35}O_{5.65}$
Bi–O(1)	3.42(2)	3.31(2)	3.14(2)
O(2)	2.17(2)	2.19(2)	2.15(1)
O(2)	2.45(2)	2.44(3)	2.45(1)
O(2)	2.25(5)	2.22(4)	—
O(2)	2.40(5)	2.51(4)	—
O(2b)	2.74(2)	2.78(3)	
O(2b)	2.27(4)	2.26(5)	
O(2b)	3.12(5)	3.19(7)	
O(3)	2.80(2)	2.71(3)	2.67(1)
O(3)	2.80(4)	2.71(5)	—
O(3)	2.83(4)	2.88(5)	—
	2.9	*2.7*	*2.7*
U/Zr–O(1)	2.19(3)	2.24(3)	2.37(1)
O(1)	2.56(5)	2.44(5)	—
O(1)	2.18(5)	2.25(5)	—
O(1b)	3.45(1)	3.45(1)	3.47(1)
O(1b)	2.26(5)	2.19(4)	2.01(1)
O(1b)	1.75(6)	1.81(4)	
O(3)	1.88(2)	1.93(2)	2.01(1)
	6.7	*6.7*	*5.3*
O(1)–O(1)	2.53(3)	2.45(4)	2.35(1)
O(1)	2.21(7)	2.26(7)	—
(O(1b))	(1.26(3))	(1.23(3))	(1.18(1))
O(1b)	2.98(6)	3.05(7)	3.07(1)
O(1b)	2.94(6)	2.95(7)	—
O(3)	2.81(3)	2.80(3)	2.94(1)
O(3)	2.85(5)	2.81(5)	—
O(3)	3.14(5)	3.16(6)	3.21(2)
O(3)	2.97(3)	3.11(3)	3.17(1)
O(3)	2.93(5)	2.93(4)	—
O(3)	3.21(5)	3.26(5)	—
O(1b)–O(3)	2.58(5)	2.55(6)	2.84(1)
O(3)	2.93(6)	3.03(7)	
(O(1b))			(2.01(1))
O(2)–O(2)	2.98(2)	2.91(3)	2.69(1)
O(2)	2.74(5)	2.73(3)	—
O(2b)	2.38(2)	2.40(3)	
O(2b)	2.13(5)	2.12(6)	
O(2b)	2.90(6)	2.86(7)	
O(3)	3.09(3)	3.14(3)	3.15(1)
O(3)	3.23(5)	3.18(4)	—
O(3)	3.14(4)	3.11(4)	
O(2b)–O(3)	3.01(2)	2.97(2)	

[a]Bond valences in italic have been calculated assuming r_0 (Bi) = 2.094, r_0 (U) = 2.075, r_0 (Zr) = 1.928.

O(3)–O distances larger than 2.8 Å are systematically observed except with O(1b). Therefore if O(3) is involved in the conduction process, it can only be through O(3)–O(1b) jumps.

The U–O network in the equatorial plane corresponding to Bi_2UO_6 is shown in Fig. 8 and 9. Short O(1)–O(1) distances are observed and are in accord with oxide migration through these sites. According to the unrealistic O(1)–O(1b) distance of 1.26(3) Å, O(1) and O(1b) sites cannot be simultaneously occupied and therefore four different U-surroundings have to be considered: Fig. 9(a), (b), (c) and (d). Type b surrounding with a linear O(3)–U–O(3) uranyl group, normal to a plane of five secondary bonds is very common in uranates such as carnotite type compounds.[16–19] Surprisingly b and d surroundings are closely related to those found in β-U_3O_8[20] and in the model proposed by Andressen for α-U_3O_8.[21] The a and b parameters of these latter compounds are close to those of Bi_2UO_6 with a tripling of b parameters (Fig. 10). According

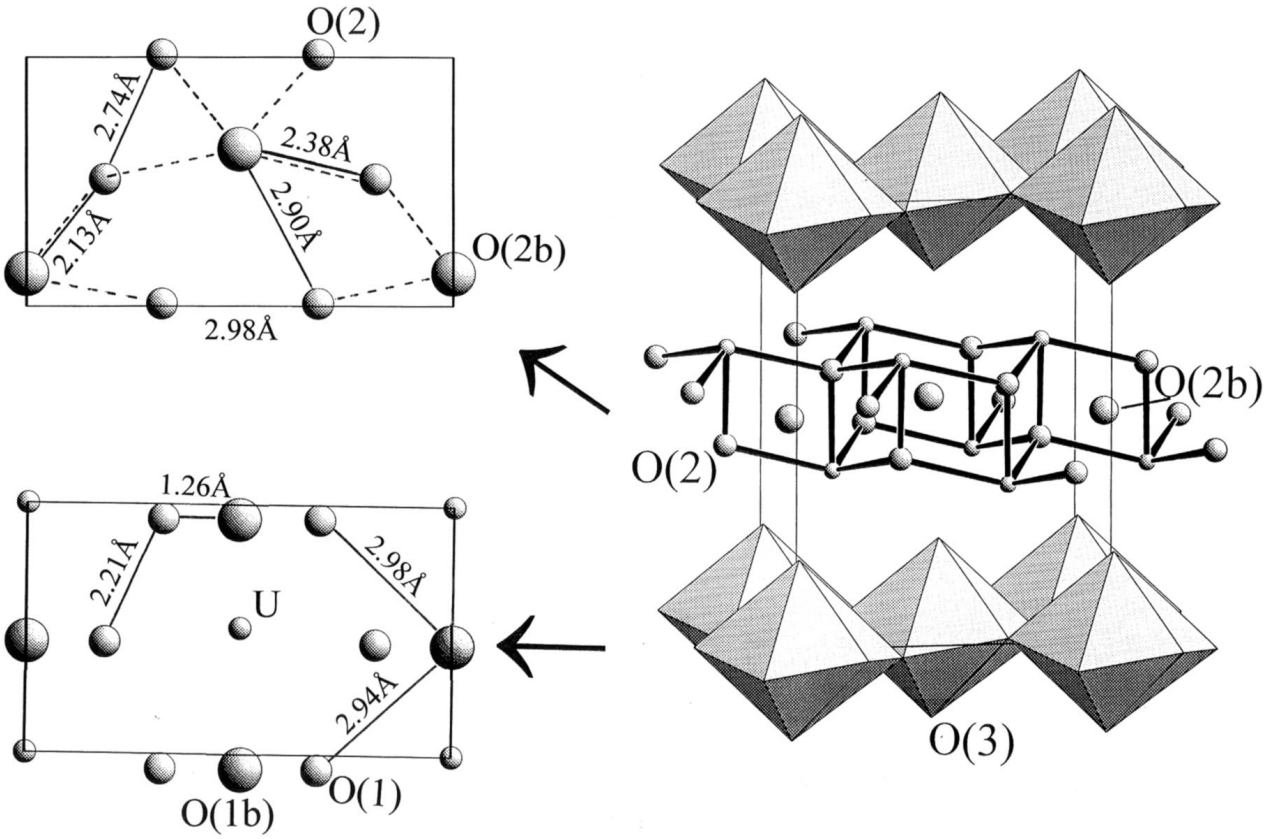

Fig. 8 Projection of oxygen atoms located in one double BiO sheet along [0 0 1] in $z=1/2$ and UO packing in $z=0$.

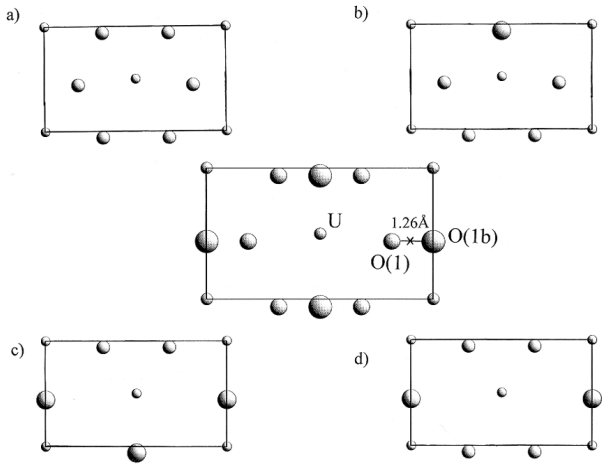

Fig. 9 UO network in the equatorial plane of the UO_4 layers of Bi_2UO_6.

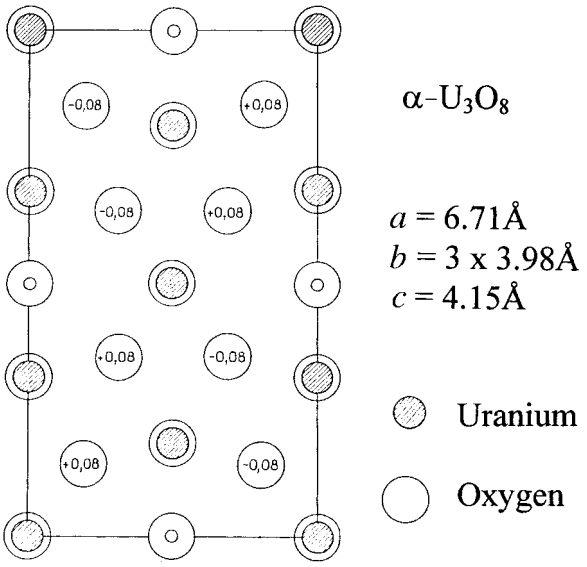

Fig. 10 α-U_3O_8 structural model proposed by Andressen.[21]

to these similarities the same oxygen packing could be proposed in Bi_2UO_6 involving a tripling of the b parameter (Fig. 11). In this model, O(1)–O(1b) bond lengths >2.9 Å, are too long to be in favour of oxygen migration *via* the O(1b) site and migration in these planes can only take place through O(1). A possible preferential migration pathway is shown by a dotted line in Fig. 11.

Similarly, for $Bi_2U_{0.65}Zr_{0.35}O_{5.65}$, a too small O(1)–O(1b) bond length of 1.18(1) Å precludes the simultaneous occupancy of these two sites. Furthermore, because of an unrealistic O(1b)–O(1b) distance of 2.01(1) two adjacent O(1b) oxygen atoms cannot occur and the same model of U–O packing as in the non-doped material can be proposed (Fig. 12).

Due to the possible ordering of uranium polyhedra, superstructures were expected. Therefore an electron microscopy study has been performed although a previous study on slice block polished Bi_2UO_6 had not revealed any superstructure phenomenon.[22]

Electron microscopy

(a) Electron diffraction. Transmission electron microscopy has been performed on the undoped Bi_2UO_6 as well as on two Zr substituted materials corresponding to $x=0.35$ and 0.45, the latter composition corresponding to the solid solution limit. Typical electron diffraction patterns corresponding to the undoped Bi_2UO_6 are shown in Fig. 13 and 14. Intense reflections confirm the basic, quasi-orthorhombic cell. However, as expected from the neutron diffraction measure-

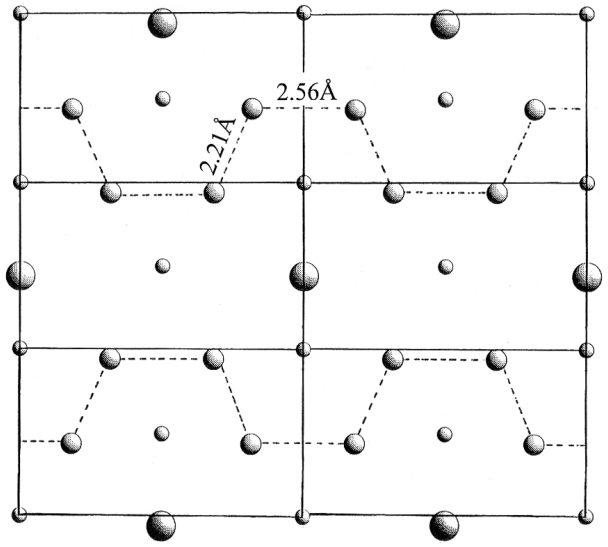

Fig. 11 A possible oxygen packing and oxygen migration pathway in the equatorial plane of the UO_4 slabs of Bi_2UO_6.

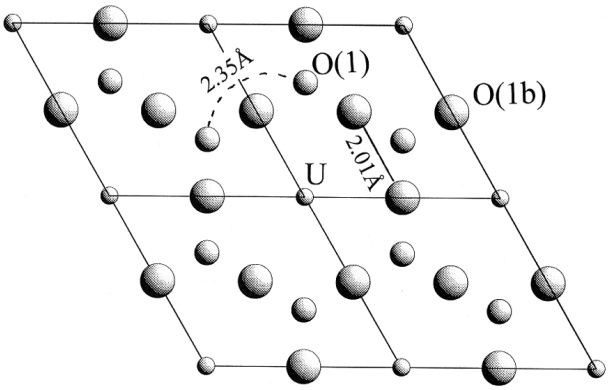

Fig. 12 UO network in the equatorial plane of the UO_4 layers of $Bi_2U_{0.65}Zr_{0.35}O_{5.65}$.

ments, weaker superstructure reflections appear. Taking into account the presence of these additional reflections along different zones, a reciprocal space can be reconstructed, which leads to a monoclinic $a \times 3b \times 2c$ supercell. The C-centering is preserved and moreover extinctions of $h0l$ reflections with $l = 2n+1$ are observed. These extinctions are evident in the [0 1 0] pattern of Fig. 14; a doubling of the c-axis, however, is not observed in this section. Taking into account these reflection conditions only two space groups qualify for this supercell: $C2/c$ and Cc.

The modulation wavelength along b is exactly equal to 3 only for a limited number of crystals. Mostly, the modulation is incommensurate and slightly smaller than 3. This incommensurability aspect is clearly visible in the [1 0 0] pattern of Fig. 13(b). The horizontal rows of superstructure reflections no longer subdivide the distance between the origin and the 0 6 0 reflection (indexed in the supercell) in three equal parts; arrows point out weak rows which are second order reflections of the incommensurate modulation along b^*. The streaking within these rows is due to (0 1 0) planar defects. Therefore, these materials should be described in a four-dimensional space group and the electron diffraction patterns can be indexed in $C2$ (0, γ, 1/2) [a non-standard setting of superspace group no. 5.4, B2 (0, 1/2, γ)].

[1 0 0] patterns of the Zr-doped material are very similar to the undoped ones [compare Fig. 15 and 13(a)]; the modulation along b^* however is systematically commensurate and the diffuse streaking along c^* seems to increase with the Zr content.

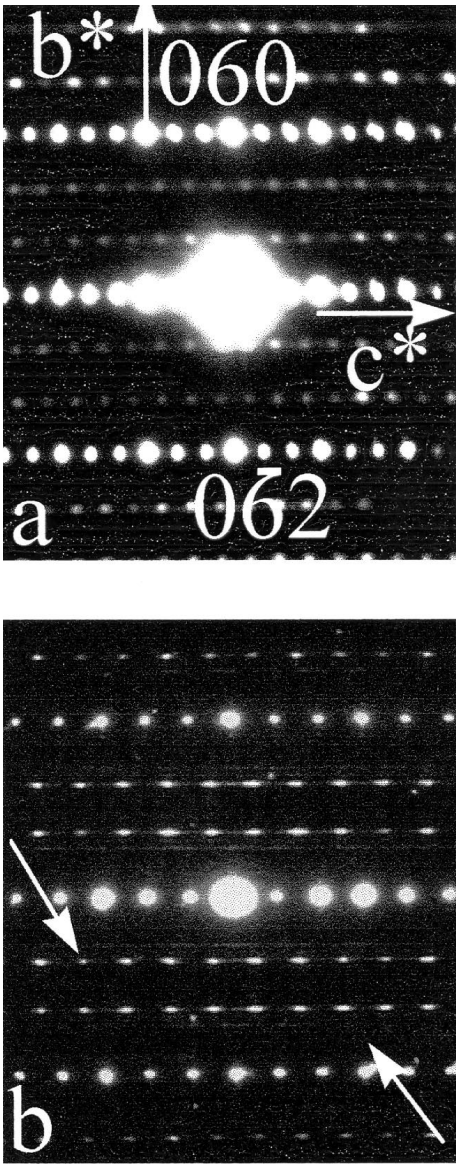

Fig. 13 [100] electron diffraction pattern (indexed in the supercell). Intense reflections confirm the basic, quasi-orthorhombic, cell. Weaker superstructure reflections related to $a \times 3b \times 2c$ supercell appear. The modulation wavelength along b (a) is exactly equal to 3 only for a limited number of crystals; (b) mostly the modulation appeared somewhat smaller than 3. Arrows point out weak streaks which are second order reflections of the incommensurate modulation along b; the presence of diffuse spots along c can be attributed to some disorder in this direction.

(b) HREM. HREM images have been obtained along different sections for the sample. The main idea is to relate the different aspects observed in diffraction (*e.g.* superstructure formation or incommensurability) to structural changes in the basic structure (what is modulating?).

The [0 1 0] pattern of Fig. 14 only reveals basic reflections and therefore the corresponding HREM images of Fig. 16(a), (b) only show the basic unmodulated structure. Image simulations using the atomic positions obtained by neutron diffraction (Table 3) reveal a good correspondence with the experimental image for a thickness of 30 Å and defocus of -800 and -400 Å respectively. In the first image [Fig. 16(a)] cations appear as bright dots with Bi^{3+} being more intense than U^{6+}. In Fig. 16(b) the contrast is reversed and cations are imaged as dark dots. This excellent correspondence between the experimental image and calculated image confirms the structural model obtained by neutrons and allows establishment of an imaging code and to identify the different atomic

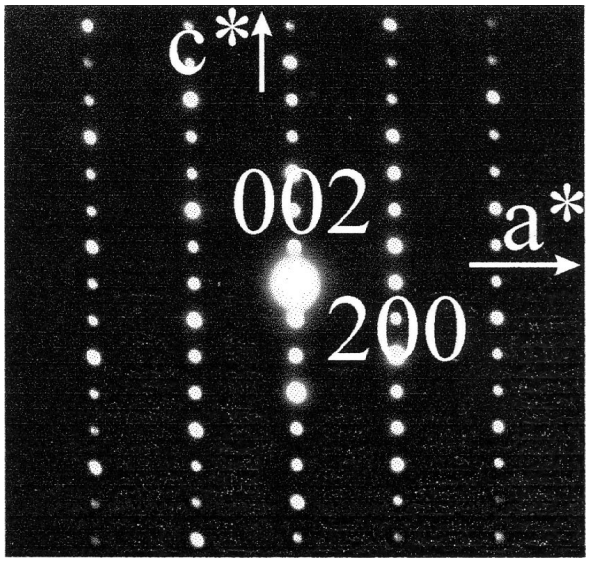

Fig. 14 [010] electron diffraction pattern (indexed in the supercell). The C lattice is preserved and moreover one notices extinctions of $h0l$ reflections with $l=2n+1$.

species. The [1 0 0] zone, imaged in Fig. 17, is the most relevant since it contains both modulation directions. The corresponding diffraction pattern is shown in Fig. 13(b). Along the *b*-axis, a modulation of about three basic units is clearly observed in most parts. Again image simulations are obtained using the basic unmodulated structure as input. Obviously no superstructure formation is to be expected in these simulations. For the very thin regions [Fig. 18(a) is an enlargement of part A in Fig. 17] the best correspondence is obtained for a thickness of 30 Å and a defocus of −100 Å [Fig. 18(b)]. The UO(1) layers appear here as very dark lines sandwiched between intense bright layers, which correspond to O(3) positions. The lines of less bright spots in between correspond to O(2b) sites. BiO(2) layers appear as less dark lines on both sides of the O(2b) sites.

The main differences between the calculated image and the experimental images of thin areas are clearly situated within the O(2b) layers; an intensity modulation appears approximately every three dots. This modulation is directly related to the superstructure formation observed in the corresponding diffraction pattern. In some crystals the modulation is indeed commensurate and equal to $3b$; in other crystals the intense dots have an average separation $<3b$, due to a mixture of three and two spacings, giving rise to an incommensurate diffraction pattern. Successive O(2b) layers are not in phase but are shifted over 1/2 of the $3b$ period (see the rectangles in Fig. 18). This alternation implies a doubling of the *c*-axis and destroys the twofold axis. The supercell remains monoclinic however, so that the only compatible symmetry would be *Cc*. Assuming the complete modulation would be due to the O(2b) ordering, a structural model corresponding to the $a\times3b\times2c$ supercell can be proposed and is shown in Fig. 19. When image simulations are performed using this commensurate supercell [Fig. 18(c)] the threefold doubling of the *b*-parameter is indeed observed within the O(2b) rows and the intensity distribution is very similar to the experimentally observed one. Incommensurate patterns are created by deviations from the threefold period (see *e.g.* part C of Fig. 17) and streaking along the c^* direction is related to the deviations from the doubling of the *c*-parameter.

In the thicker parts of the sample (zone B, Fig. 17), a variation of contrast in O(3) layers is also observed: groups of three bright dots are indicated by arrows. It is to be expected that changes in the O(2b) configuration will influence

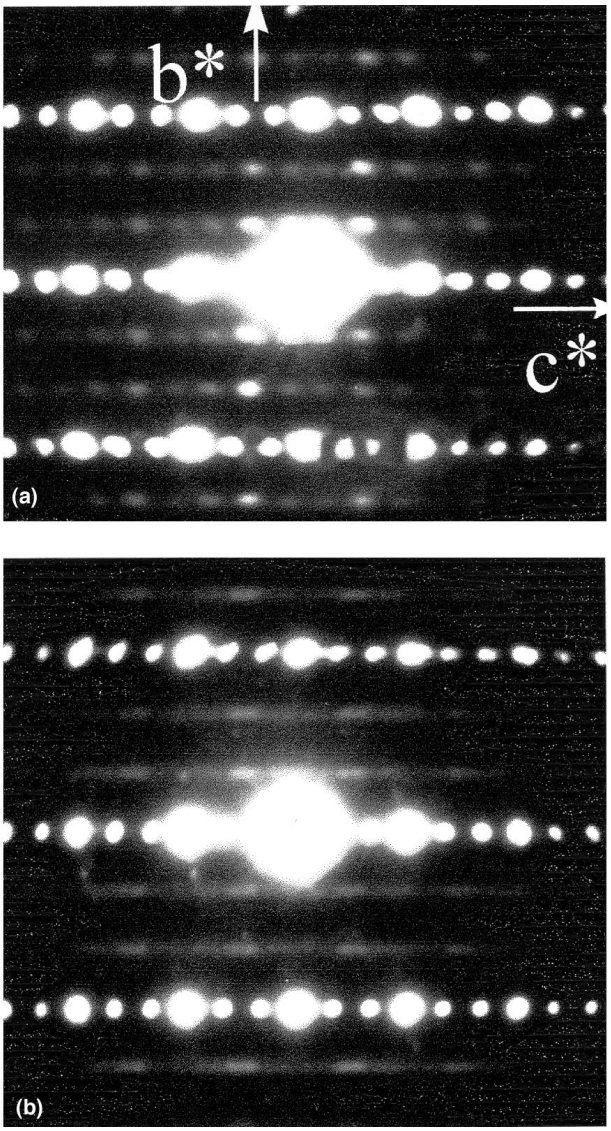

Fig. 15 [100] electron diffraction pattern of $Bi_2U_{1-x}Zr_xO_{6-x}$ compounds. (a) $x=0.35$, (b) $x=0.45$. They are very similar to the Bi_2UO_6 one. However, the modulation along *b* is systematically commensurate and it is seen that the intensity of the diffuse spots along *c*, related to some disorder in this direction, increases with the zirconium content.

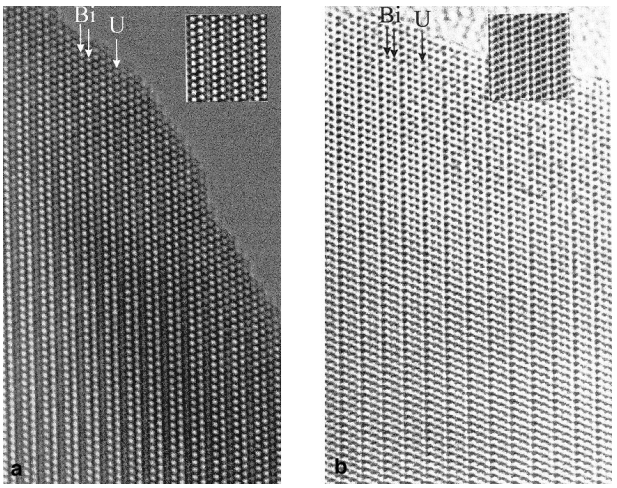

Fig. 16 Bi_2UO_6 [010] HREM corresponding to the electron diffraction pattern of Fig. 15 and image simulation performed on the basis of the atomic positions of Table 3. (a) For a thickness of 30 Å and defocus of −800 Å, the cations appear as bright dots; (b) for a thickness of 30 Å and defocus of −400 Å, the cations appear as dark dots.

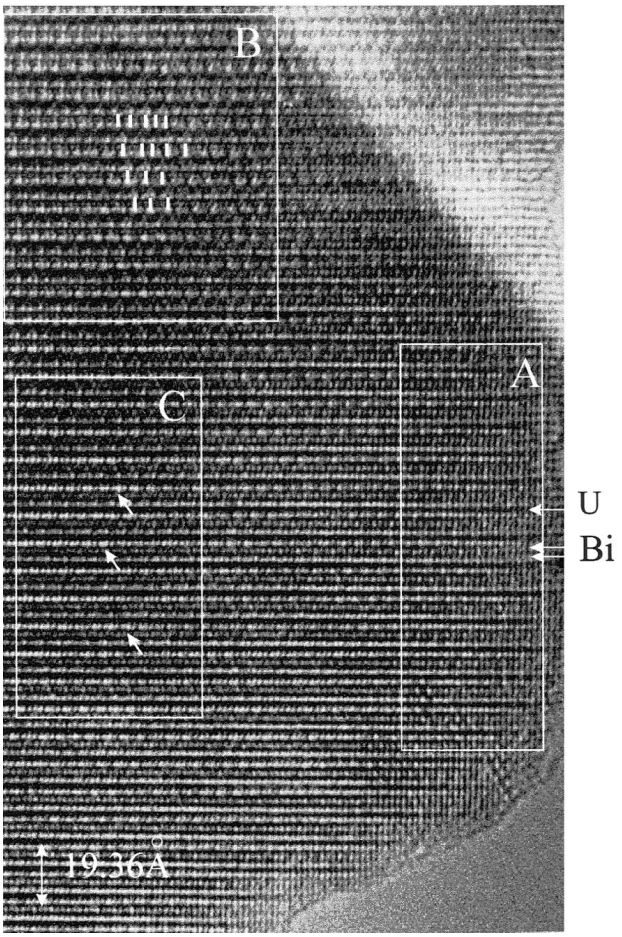

Fig. 17 Bi_2UO_6 [100] HREM corresponding to the electron diffraction pattern of Fig. 14(b). In the thicker part of the sample (zone B), a variation of contrast in O(3) layers is also observed (arrows): a group of three bright dots are outlined. In the thicker part, incommensurate phenomena are also highlighted (zone C): irregular orders between O(2b) sites are clearly observed.

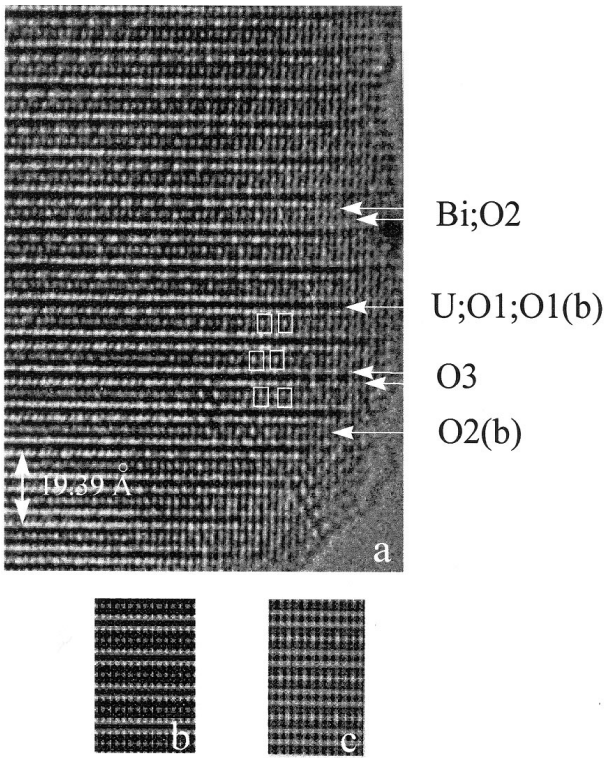

Fig. 18 (a) Enlargement of zone A of Fig. 17. An ordering of the O(2b) site is observed (rectangle) and is likely to be responsible for the superstructure. (b) Calculated image for a thickness of 30 Å and a defocus of −100 Å, without superstructure consideration. (c) Calculated image assuming the modulation for a thickness of 30 Å and a defocus of 80 Å.

the O(3) layers. Depending on thickness and focus, these effects are highlighted.

From these HREM observations, it is clear that the modulations in Bi_2UO_6 are primarily related to a complex ordering at the O(2b) sites. Furthermore a related ordering of the oxygen atoms located in the equatorial UO planes cannot be excluded. These modulations are maintained in all Zr-substituted materials where vacancies are available on the O(2b) site.

This complex, defective and incommensurate ordering indicates why a further refinement of the neutron data in the supercell was not possible.

The electron diffraction and HREM study are consistent with the hypothesis of an extra oxygen. It shows that the phenomenon which generates the commensurate or incommensurate superstructures takes place at the level of the O(2b) layer and it influences the adjacent layers.

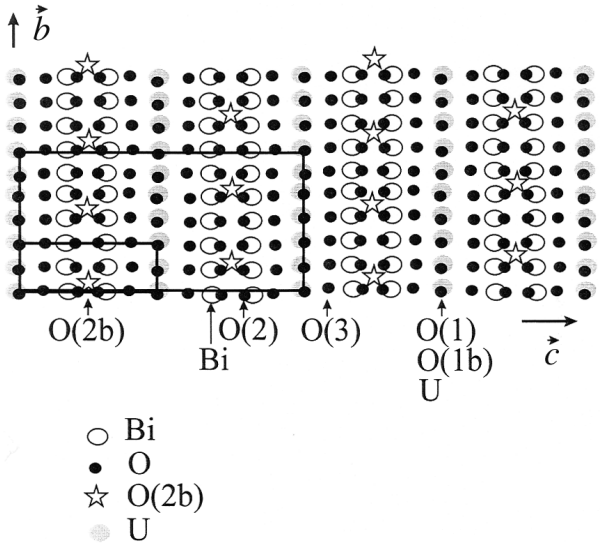

Fig. 19 Proposed schematic structural model corresponding to the $a \times 3b \times 2c$ supercell.

Conclusion

A $Bi_2U_{1-x}Zr_xO_{6-x}$ solid solution has been evidenced for $0 \leqslant x \leqslant 0.40$. A monoclinic form extends in the range $0 \leqslant x \leqslant 0.20$ and a related trigonal high-temperature Bi_2UO_6 form is stabilised at room temperature for higher substitution ratios. A rather good approximation of the basic structure has been obtained by neutron diffraction.

The two dimensional properties of these materials have been demonstrated.

(i) The presence of interstitial O(2b) oxide is essential to understand the conduction in the monoclinic forms and two preferential oxygen migration pathways in these forms can be proposed: the first through Bi–O slabs and the second in the equatorial plane of the 'UO' packing.

(ii) In the related trigonal form, O(2b) is vacant and conduction is only allowed through 'UO' planes.

This study was completed by electron diffraction microscopy that revealed incommensurate modulations due to ordering of O(2b) sites.

Acknowledgements

The Institut Laue Langevin (Grenoble, France) and the EMAT laboratory (Antwerp, Belgium) are acknowledged for providing neutron and electron microscopy facilities respectively. Professor Mairesse is thanked for useful discussions.

References

1 J. C. Boivin, R. N. Vannier, G. Mairesse, F. Abraham and G. Nowogrocki, *ISSI Lett*., 1992, No. 4.
2 G. Mairesse, in *Fast Ion Transport in Solids*, ed. B. Scrosati, Kluwer, Dordrecht, 1993, p. 271.
3 S. Lazure, R. N. Vannier, G. Nowogrocki and G. Mairesse, *Solid State Ionics*, 1996, **90**, 117.
4 F. Abraham, M. F. Debreuille-Gresse, G. Mairesse and G. Nowogrocki, *Solid State Ionics*, 1988, **28/30**, 529.
5 N. Baux, R. N. Vannier, G. Mairesse and G. Nowogrocki, *Solid State Ionics*, 1996, **91**, 243.
6 N. Bonanos, *Mater. Res. Bull.*, 1989, **24**, 1531.
7 A. S. Koster, J. P. P. Renaud and G. D. Rieck, *Acta Crystallogr.*, *Sect. B*, 1975, **31**, 127.
8 O. Théry, R. N. Vannier, C. Dion and F. Abraham, *Solid State Ionics*, 1996, **90**, 105.
9 O. Théry, C. Kinowski, R. N. Vannier and F. Abraham, to be published.
10 J. Rodriguez-Carjaval, Program Fullprof, version 2.4, 1993.
11 M. S. Islam, S. Lazure, R. N. Vannier, G. Nowogrocki and G. Mairesse, *J. Mater. Chem*., 1998, **8**, 655.
12 I. D. Brown and D. Altermatt, *Acta Crystallogr.*, *Sect. B*, 1985, **41**, 244.
13 A. Demourgues, F. Weill, B. Darriet, A. Wattiaux, J. C. Grenier, P. Gravereau and M. Pouchard, *J. Solid State Chem.*, 1993, **106**, 317.
14 A. Demourgues, F. Weill, B. Darriet, A. Wattiaux, J. C. Grenier, P. Gravereau and M. Pouchard, *J. Solid State Chem.*, 1993, **106**, 330.
15 J. D. Jorgensen, B. Dabrowski, Shiyou Pei, D. R. Richards and D. G. Hinks, *Phys. Rev. B*, 1989, **40**, 2187.
16 F. Abraham, C. Dion and M. Saadi, *J. Mater. Chem.*, 1993, **3**, 459.
17 F. Abraham, C. Dion, N. Tancret and M. Saadi, *Adv. Mater. Res.*, 1994, **1/2**, 511.
18 M. Gasperin, *Acta Crystallogr.*, *Sect. C*, 1988, **44**, 415.
19 N. Tancret, S. Obbade and F. Abraham, *Eur. J. Solid State Inorg. Chem*., 1995, **32**, 195.
20 B. O. Loopstra, *Acta Crystallogr.*, *Sect. B*, 1970, **46**, 656.
21 A. J Andressen, *Symp. Reator Mater.*, Stockholm, 1959.
22 D. White and S. Ramdas, *Ultramicroscopy*, 1989, **31**, 124.

Paper 8/05829F